Corrosion inhibition of carbon steel in hydrochloric acid: Elucidating the performance of an imidazoline-based surfactant

K. Kousar[a], M.S. Walczak[a], T. Ljungdahl[b], A. Wetzel[b], H. Oskarsson[b],

P. Restuccia[c], E.A. Ahmad[c], N.M. Harrison[c], R. Lindsay[a,d]

[a]*Corrosion and Protection Centre, Department of Materials, The University of Manchester, Sackville Street, Manchester, M13 9PL, UK.*

[b]*Nouryon, Hamnvägen 2, SE-444 85 Stenungsund, Sweden.*

[c]*Department of Chemistry and Institute for Molecular Science and Engineering, Imperial College London, White City Campus, 80 Wood Lane, London W12 0BZ, UK*

[d]*Photon Science Institute, The University of Manchester, Oxford Road, Manchester, M13 9PL, UK.*

Corresponding Author:

Robert Lindsay

Tel: +44 161 306 4824

Fax: +44 161 306 4865

Email: robert.lindsay@manchester.ac.uk

Abstract

A combination of electrochemical measurement and interface analysis have been applied to characterise the interaction of OMID, an exemplar imidazoline-based corrosion inhibitor, with carbon steel in 1 M hydrochloric acid. Corrosion inhibition efficiency data indicate that excellent performance is achieved well below the critical micelle concentration. High resolution X-ray photoelectron spectra demonstrate that, as the corrosion rate decreases, the interface evolves towards one comprising OMID bound to film-free carbon steel. This latter result provides key input for those researchers attempting to predict corrosion inhibitor functionality through atomic scale interfacial modelling, and so identify next generation chemistries.

Keywords: Carbon steel (A); Polarization (B); XPS (B); Acid inhibition (C)

1. Introduction

Acid-driven corrosion is a major concern for a number of industries, including oil and gas production, and effective methods to mitigate this phenomenon are of the utmost importance. One widely applied approach is to add surfactants to the corrosive medium to effect corrosion inhibition through binding to the substrate [1,2]. N-containing amphiphilic organic species are extensively employed for this purpose due to their excellent corrosion inhibition properties. Detailed understanding of their functionality, however, is quite limited, restricting knowledge-based advances. Here, we make a substantive contribution to this topic through studying the performance and interfacial chemistry of an exemplar imidazoline-based surfactant [3–11] for corrosion inhibition of carbon steel in 1 M HCl; the structure of this species, which will henceforth be referred to as OMID, is illustrated the Figure 1.

Published literature is consistent with OMID being a high performing corrosion inhibitor (CI) for carbon steel in strong acids [7,8,10,11]. For example, Olivares-Xometl *et al.* report an inhibition efficiency (η%) of 91% at a concentration of 100 ppm (~ 0.03 mM) in 1 M hydrochloric acid (HCl) at room temperature [8]. In an analogous environment, we have recently demonstrated that η% ~ 97% at an OMID concentration of 0.18 mM, which is the critical micelle concentration (CMC) for this species under these conditions [11]; η% was determined at CMC, as it is typically expected that a surfactant CI will almost certainly be performing optimally at this concentration [2].

Concerning the chemistry of the inhibited OMID/carbon steel interface in 1 M HCl, Olivares-Xometl *et al.* applied X-ray photoelectron spectroscopy (XPS) to gain insight [7,8]. They concluded that adsorbed OMID is bound to a substrate terminated by both Fe^{3+} oxide (Fe_2O_3) and chloride ($FeCl_3$). This result, however, is likely to be compromised, as no precautions were seemingly taken to avoid post immersion oxidation. In the current study, we overcome this issue, applying an approach developed in our group to acquire XPS spectra from air-sensitive inhibited interfaces [12]. Building on Ref. [11], we systematically explore the corrosion inhibition performance of OMID for carbon steel in 1 M HCl as a function of

concentration, using both potentiodynamic polarisation (PDP) and linear polarisation resistance (LPR) measurements. For selected OMID concentrations, we correlate corrosion inhibitor efficiency with interface chemistry determined from XPS; *ab initio* calculations are employed to support line shape selection for fitting of selected XPS core levels (Cl 2p).

2. Materials and methods

Carbon steel samples (10 mm × 10 mm × 1.5 mm) supplied by RCSL Corrosion Monitoring Ltd (see Ref. [11] for details of nominal composition) were employed for the acquisition of both electrochemical and XPS data. For the former measurements, a sequence of SiC papers (400 grit, 600 grit, 800 grit) were used to grind the samples, following mounting in epoxy resin to expose a 1.0 cm^2 area. Subsequently, ethanol and de-ionised water were used to rinse the samples, and then they were dried with flowing air. Samples for XPS were also ground initially with SiC papers (400 grit, 600 grit, 800 grit, 1200 grit, 2400 grit, 4000 grit), and then polished to a mirror finish with diamond paste (1 μm). Acetone and de-ionised water were used to degrease these samples, after which they were dried as above. De-ionised water was used to dilute 10.2 M HCl (analytical grade, Fisher Scientific) to produce 1 M HCl, and OMID was added to form a series of *1 M HCl + x mM OMID* solutions, where *x* lies in the range of 0 mM to 0.1 mM. The OMID (97.7% purity) employed in this study had been synthesised and characterised according to procedures outlined in Ref. [11], including determination of both its CMC (0.18 mM) and propensity for hydrolysis in 1 M HCl; no evidence of hydrolysis was found for the current experimental conditions. All of the data presented below, with the exception of those from polished samples, were acquired from samples subsequent to immersion for 4 h in naturally aerated *1 M HCl + x mM OMID* at room temperature (25°C).

PDP and LPR data were acquired in a 1 L glass cell that contained the desired *1M HCl + x mM OMID* solution. A three-electrode cell setup was employed, comprising a working electrode (carbon steel), a counter electrode (platinum), and a reference electrode (saturated calomel electrode) that was located in a separate vessel connected to the 1 L cell through a Luggin probe. LPR (PDP) data were recorded with a computer controlled potentiostat (Ivium

Compactstat), using the range -10 mV to +10 mV (-250 mV to +250 mV) with respect to open circuit potential (OCP), and employing a scan rate of 10 mV/min (120 mV/min). Corrosion rate values were determined from LPR measurements, using standard methodology [13], with the Stern-Geary coefficients being obtained from corresponding PDP data; relevant equations are provided in Supplementary Material. PDP graphs are shown without the so-called IR drop correction, which is essentially a feature of finite solution resistance [14].

A Zeiss EVO-50 SEM was used to evaluate substrate morphology post immersion. Images were acquired from samples only subjected to LPR measurements, as the larger polarisation experienced during PDP may induce the alteration of substrate features. Adhered corrosion products were removed from the substrate prior to imaging through gentle scrubbing followed by washing with de-ionised water and acetone, and drying under a stream of air.

A Kratos Axis Ultra spectrometer, equipped with an Al Kα X-ray source ($h\nu$ = 1486.6 eV, $\Delta h\nu$ ~ 0.16 eV) and a 165 mm hemispherical energy analyser, was used for XPS measurements. To mitigate post-immersion oxidation, samples were immersed in *1 M HCl + x mM OMID* solutions inside an inert atmosphere (N_2) glove box attached to the load lock system of the XPS spectrometer [12]. Following removal of a sample from solution, it was exposed to a flow nitrogen to prevent solution evaporation from the substrate surface and resulting physical deposition of non-volatile solution constituents. Data acquisition was performed at normal emission ($\theta_E = 0°$), using an ~ 3 mm × ~ 2 mm analysis area. Pass energies of 80 eV and 20 eV were used to record overview spectra and higher resolution single core level spectra, respectively. Samples were mounted on a sample plate using double sided vacuum compatible adhesive carbon tape, and exposed to a flood source of low energy electrons (≤ 3 eV) to avoid charge accumulation during measurements. The metallic Fe peak at a binding energy (BE) of 706.7 eV was used to calibrate (± 0.1 eV) the spectra [15].

Spectral fitting was carried out using CasaXPS software [16]. As regards Fe 2p spectra, only the Fe $2p_{3/2}$ component was considered, in accordance with previous work [17,18]. To fit the

Fe^{2+} and Fe^{3+} states, multiplets comprising 3 and 4 Gaussian-Lorentzian (GL) line shape functions, respectively, and up to two broader GL line shape functions for satellite peaks have been employed [17–19]. The GL function uses a single adjustable parameter to define the line shape, i.e. GL(p). p, which lies in the range $0 \leq p \leq 100$, describes the degree of Gaussian-Lorentzian mixing, where GL(100) (GL(0)) is a pure Lorentzian (Gaussian) line shape. All of the other photoelectron peaks were also modelled with GL line shape functions, except for the metallic iron (Fe^0) Fe 2p core level and the Cl 2p signal assigned to adsorbed chlorine atoms (see below). These peaks were modelled with a Gaussian-convoluted Lorentzian based asymmetric (LF) function, which uses four adjustable parameters to define its line shape, i.e. LF(α, β, w, m) [20]. α and β specify the spread of the tail to higher and lower BE, respectively, relative to the Lorentzian function maximum. The degree of peak asymmetry is defined by the difference between α and β, and w is a damping factor to limit the range of asymmetry. m describes the width of the Gaussian used for convolution. Shirley-type functions were used to account for inelastically scattered background electrons in all of the presented data [21].

Application of an asymmetric line shape is well known for metallic substrates [22,23], but requires further justification for adsorbed species, i.e. atomic chlorine in this case. To this end, following an approach detailed in Ref. [24], hybrid exchange density functional theory (DFT) has been employed, using the CRYSTAL 17 program [25,26], to compute pertinent projected electronic density of states (PDOS). These calculations used all electron triple valence basis sets with polarisation, i.e. 8-64111d41G for iron atoms and 86-311G with the addition of a diffusive d-orbital for chlorine atoms.

3. Results and discussion

PDP curves, for a series of OMID concentrations (0 mM to 0.1 mM) in 1 M HCl, are depicted in Fig. 2. It can be observed that the addition of OMID inhibits corrosion as the current density systemically shifts to lower values with increasing concentration. Also, there are no significant changes in the corrosion potential as a function of OMID concentration. Consistent with previous work [7,8,10], this behaviour is indicative of OMID behaving as a mixed-type CI,

with both the anodic and cathodic reactions being similarly impeded [27]. Furthermore, the gradients of the anodic and cathodic reactions are typical of activation-controlled kinetics, i.e. all polarisation curves exhibit approximately Tafel-like behaviour [13]. The numerical values of these gradients are listed in Table S1 of Supplementary Material. For the anodic branch, there is no significant variation with OMID concentration, but there is a systematic increase for the cathodic branch for OMID concentrations ≥ 0.001 mM. This behaviour may indicate a change in mechanism of the cathodic reaction, suggesting inhibition is not achieved through simply blocking active anodic/cathodic sites.

The corrosion rate of carbon steel in *1 M HCl + x mM OMID*, determined from LPR measurements after immersion for 4 h, is plotted (red markers) as a function of increasing OMID concentration in Fig. 3; Table S1 in Supplementary Material lists the Stern-Geary (B) coefficients, and other relevant data, employed to calculate these corrosion rates. Evidently, increasing the concentration of OMID in bulk solution shows an essentially asymptotic decrease in the corrosion rate towards a limiting value. The uninhibited corrosion rate (*1 M HCl + 0 mM OMID*) was determined to be 3.75 ± 0.07 mm/y, which reduced to 0.13 ± 0.01 mm/y for *1 M HCl + 0.1 mM OMID*.

SEM images of carbon steel samples are also consistent with a significant reduction in corrosion rate for *1 M HCl + 0.1 mM OMID*. Fig. 4 shows representative SEM images of (a) a polished sample, (b) a sample following immersion in *1 M HCl + 0 mM OMID*, and (c) a sample following immersion in *1 M HCl + 0.1 mM OMID*. Both the polished sample and that immersed in *1 M HCl + 0.1 mM OMID* display a similar morphology, with polishing lines being clearly evident. In contrast, for the sample immersed in *1 M HCl + 0 mM OMID,* the surface finish appears to be significantly degraded, i.e. roughened as a result of corrosion. These qualitative observations support the quantitative changes in corrosion rate determined from electrochemical measurements. Furthermore, they demonstrate that localised corrosion (e.g. pit formation) is not an issue for the substrate in this environment, which would undermine the performance of OMID as an effective CI.

To facilitate comparison of the performance of OMID with related studies and/or other CIs, corrosion inhibition efficiency (η%) is also plotted (blue markers) as a function of increasing OMID concentration in Fig. 3. This widely applied figure of merit for corrosion inhibition is defined as:

$$\eta\% = \frac{(U - I)}{U} \times 100. \quad (1)$$

U (I) is the uninhibited (inhibited) corrosion rate. Examining Fig. 3, η% ~ 96% at an OMID concentration of 0.01 mM, increasing only slightly to ~ 97 % at 0.1 mM. Given that reagents with η% > 95% are typically considered to be high performing CIs [28], it can be concluded that OMID is performing as expected in 1 M HCl [7,8,11]. Interestingly, the inhibition efficiency at 0.01 mM is almost identical to that found for OMID at CMC (0.18 mM) in this environment [11], i.e. an almost optimal inhibition performance is achieved for OMID at a concentration more than one order of magnitude less than CMC. This result is consistent with other studies, where it is reported that the maximum corrosion inhibition efficiency is achieved well below CMC [29–31]. Researchers suggest that this phenomenon is connected to the so-called critical surface aggregation concentration (CSAC) of a surfactant, which is often significantly lower than the CMC [2,32]; CSAC can be interpreted as the surfactant concentration in bulk solution where a complete contact layer is formed on a solid substrate.

Turning to interfacial chemistry, Fig. 5 shows a series of overview XPS spectra acquired from carbon steel samples subsequent to immersion in *1 M HCl + x mM OMID*; a spectrum of a polished sample is also displayed. Focusing on the latter spectrum, as indicated by the annotation, prominent features arising from the Fe 2p, O 1s and C 1s core levels are apparent. In accord with earlier studies [17,18,33], the Fe signal can be attributed to the carbon steel substrate, O to both a surface oxidic film and adsorbed species, and C to adventitious surface contamination.

Immersion in uninhibited 1 M HCl solution (i.e. *1 M HCl + 0 mM OMID*) leads to noticeable changes in the corresponding overview XPS spectrum in Fig. 5. Firstly, there is an obvious loss in intensity of the O 1s feature, suggesting depletion of the surface oxidic film. Peaks assigned to the Cl 2s and 2p core levels also appear, which can be attributed to interaction of the substrate with Cl anions in the acidic solution. The signal ascribed to Cu 2p almost certainly arises from a minority substrate component, which is revealed following anodic dissolution of Fe through corrosion [18].

Further modification of the overview XPS spectra in Fig. 5 are apparent following immersion in 1 M HCl solutions containing various concentrations of OMID. Most importantly, a N 1s peak appears, which is consistent with OMID binding to the carbon steel substrate. Moreover, an increase in the intensity of this nitrogen signal is observed as the concentration of OMID is increased. This trend suggests that, similar to other organic species employed to inhibit corrosion at low pH, OMID adsorptions follows some kind of adsorption isotherm [27,28]. In addition to the rise of the N 1s signal, there is a reduction in intensity of the peaks assigned to oxygen and chlorine, suggesting further interfacial modifications as the inhibition efficiency of OMID increases. The Cu 2p feature also diminishes, becoming absent in the presence of 0.1 mM OMID, which can most simply be correlated with reduced interfacial enrichment of Cu at lower corrosion rates (higher corrosion inhibition efficiencies).

More detailed insight into interfacial chemistry can be gained from higher resolution XPS spectra of individual core levels. Fig. 6 shows a series of N 1s core level XPS spectra acquired from carbon steel samples, subsequent to immersion in *1 M HCl + x mM* OMID, along with one from a polished sample; it should be noted that the N 1s signal is employed as the key indicator of OMID adsorption, as C 1s XPS data are inconclusive due to the persistent presence of adventitious carbon [34]. Best fits to these spectra are also displayed; the BE and full with half maximum (fwhm) of each GL line shape function is listed in Supplementary Material (Table S2). Concerning the spectrum of the polished substrate, no N 1s features are evident,

but two peaks, located at binding energies of 397.5 eV and 399.7 eV, appear following immersion in uninhibited 1 M HCl. Analogous to the Cu 2p signal in the overview spectra (see Fig. 5), it is proposed that these peaks arise from minority substrate components (labelled as N^1 and N^2), that are enriched at the surface through anodic dissolution of the Fe matrix. This suggestion is supported by the diminution of the N^1 feature at BE = 397.5 eV as the concentration of OMID, and hence corrosion inhibition efficiency, increases.

The N 1s related intensity in the vicinity of BE = 399.7 eV in Fig. 6 increases with OMID concentration, broadening and shifting to somewhat higher BE. On this basis, it is concluded that the initial peak, assigned to a minor substrate component (N^2), is replaced by signal from adsorbed OMID. Consistent with analysis for carbon steel immersed in *1 M HCl + 0.18 mM* OMID in Ref. 11, where fitting and interpretation of the N 1s signal is discussed in detail, 5 GL line shape functions have been used to fit this feature. Briefly, it is concluded [11] that these 5 components originate from the presence of two singly protonated forms of adsorbed OMID; in bulk 1 M HCl solution the OMID head group is expected to be doubly protonated [11]. These two singly protonated species are shown in Fig. 6, along with peak assignments. Protonation occurs at either the primary amine group ($-NH_2 \rightarrow -NH_3^+$) or imine group ($>C=N- \rightarrow >C=NH^+-$), with the latter being the major adsorbed component; the tertiary amine group ($-N<$) remains unprotonated, and so is common to both species depicted in Fig. 6.

Fig. 7 shows experimental Fe 2p, O 1s and Cl 2p core level XPS spectra, and the corresponding best fits, acquired from carbon steel samples, subsequent to immersion in *1 M HCl + x mM* OMID, as well as from a polished sample; line shape functions, BEs, and fwhms of the various peaks are listed in Supplementary Material (Tables S3, S4, and S5). Focusing initially of the spectra acquired from the polished substrate, the presence of both $Fe^{2+/3+}$ multiplet states and satellites, in tandem with a feature for metallic Fe (Fe^0), as well as O1s peaks assigned to oxide (labelled O^{2-}; BE ~ 530.0 eV) and hydroxide (labelled OH^-; BE ~ 531.0 eV), are consistent with a thin oxidic film terminating the substrate [17,18,33]. The three higher BE O 1s components, labelled O^1, O^2, and O^3, are ascribed to a combination of adsorbed OH (O^1) and

adventitious RC_xO_y (O^1, O^2, and O^3) species [17,18,33]; it should be noted that in earlier work from our group, this region of the O 1s spectrum was fitted with 2 components (O^1 and O^2), but 3 components are currently preferred, as fitting is found to be more consistent.

Following immersion in uninhibited 1 M HCl, features arising from cationic iron in the Fe 2p spectrum are generally diminished, with those for Fe^{2+} being entirely quenched. The peaks attributed above to O^{2-} and OH^- are also absent in the corresponding *1 M HCl + 0 mM* OMID O 1s data. Conversely, a significant Cl 2p signal appears, which is fitted with a single spin-orbit split doublet; the Cl $2p_{3/2}$ component, labelled Cl_{salt} in Fig. 7 (c), has a BE of 199.1 eV. In accord with previous work, these changes are concluded to be associated with the replacement of the oxidic termination on the polished sample by a thin surface film of ferric chloride ($FeCl_3$) in 1 M HCl [17,18]. This interpretation is supported by a relative increase in intensity of the Fe 2p profile around BE ~ 715.6 eV, which can be associated with the presence of a Fe^{3+} satellite that has been observed in spectra acquired from bulk $FeCl_3$ [35].

In the presence of OMID, the Fe 2p core level profiles in Fig. 7 (a) evolve further as a function of concentration. More specifically, the Fe^{3+} contribution is continuously reduced, until there is only a peak arising from metallic iron (Fe^0) for *1 M HCl + 0.1 mM* OMID, where $\eta\% \sim 97\%$. The Cl 2p XPS data also vary with increasing OMID concentration, with a second spin-orbit split doublet being introduced to achieve acceptable fitting. This additional signal is assigned to adsorbed chlorine atoms [17,18]; the Cl $2p_{3/2}$ component of this doublet is labelled Cl_{ads} in Fig. 7 (c). Regarding the O 1s data in the presence of OMID, as shown Fig. 7 (b), each spectrum is fitted with the same 3 components, labelled O^1, O^2, and O^3. Given that these features are primarily attributed to adventitious RC_xO_y species, observed variations are not discussed further.

As mentioned in the preceding section, asymmetric LF line shape functions have been employed to fit Cl_{ads} signals in Fig. 7 (c). The rationale for applying this line shape is based on a recent study examining the adsorption of atomic O or S on Fe(110) [24], where it was

demonstrated through DFT calculations that significant mixing of substrate and adsorbate states results in a finite PDOS around the Fermi level (E_F). This electronic coupling produces an adsorbate XPS core level profile similar to that found for metals, i.e. asymmetric with a tail to higher BE [22,23]. To verify that Cl_{ads} hybridises similarly with iron, DFT calculations have been performed for a (2x2) ordered overlayer of atomic chlorine on Fe(110). Figure 8 depicts this structure, as well as the associated projected density of states, DFT-PDOS (-2 eV $\leq E_F \leq$ 2 eV) computed following structure optimisation. As observed previously for both O and S adsorbed on Fe(110) [24], no band gap is evident for either Fe or Cl around E_F; Cl/Fe1 DFT-PDOS ratio is ~ 0.2 at E_F. On this basis, it is concluded that the Cl 2p core level XPS profiles for Cl_{ads} should exhibit asymmetry, and so be fitted with LF line shapes.

Illustrating our interpretation of the XPS data, Fig. 9 provides a cartoon of the evolution of the carbon steel interface as a function of environment. Moving from left to right, the iron oxide/hydroxide film, displayed by the polished substrate, is replaced by an iron chloride salt film following immersion in *1 M HCl + 0 mM* OMID. As the concentration of OMID increases, the salt film coverage is reduced, becoming entirely absent for *1 M HCl + 0.1 mM* OMID ($\eta\%$ ~ 97%), i.e. the highly inhibited interface comprises OMID bound to film-free surface. For *1 M HCl + ≤ 0.005 mM* OMID, the surface is shown to be laterally heterogenous, consisting of filmed and film-free domains. Given that the XPS measurements do not provide any lateral spatial resolution, this model requires justification. Our argument centres upon the asymmetry of the Cl 2p XPS line shape for Cl_{ads} being independent of OMID concentration (see Table S5), suggesting that this species always bonds in a similar manner to the substrate, i.e. adsorbs on film-free areas. If an appreciable fraction of Cl_{ads} was located atop the iron chloride film at lower OMID concentrations, a change in core level asymmetry would be expected, resulting from a change in adsorbate/substrate electronic coupling.

Comparing the results presented here with previous work, the development of the interface depicted in Fig. 9 approximates rather well to that reported by some of the current authors for the same substrate/solution combination in the presence of another corrosion inhibitor, 2-

mercaptobenzimidazole [17,18]. Most importantly, it is concluded for both corrosion inhibitors that the well inhibited interface is film-free; this information is essential for researchers attempting to model such interactions at the atomic scale.

One difference that does distinguish the present study from Refs. [17,18] is the use of an asymmetric line shape for fitting the Cl 2p signal from Cl_{ads}, and the resulting deduction that the interface is laterally heterogenous for *1 M HCl + ≤ 0.005 mM* OMID. In the earlier work, symmetric GL line shapes were employed to fit all of the Cl 2p components, including those corresponding to Cl_{ads}. Returning to these fits, it has been found that an asymmetric line shape could also have been applied, but poorer signal-to-noise, partially a result of a lower Cl_{ads} coverage, prevents unique discrimination.

In another recent study of the corrosion inhibition of carbon steel in 1 M HCl by ammonium-based ionic liquids [36], steps were also undertaken to avoid post immersion oxidation prior to acquisition of XPS data. Similar to our work, they report that the signal from cationic Fe was very much reduced on well-inhibited substrates; the remanent $Fe^{2+/3+}$ signal is almost certainly a result of the corresponding corrosion inhibition efficiency being apparently somewhat lower ($\eta\% < 90\%$) than that reported here ($\eta\% \sim 96\%$) for an entirely film-free surface termination. In sharp contrast, other contemporaneous XPS studies (e.g. [37–39]) of corrosion inhibition of carbon steel in 1 M HCl suggest that surface oxides persist at high corrosion inhibition efficiencies. These studies are, however, almost certainly compromised by an apparent lack of effort to prevent exposure to the laboratory atmosphere during sample transfer to the XPS instrument.

Finally, we would like to comment on the role of Cl_{ads} in achieving excellent corrosion inhibition efficiency. It is established, at least for some organic species, that the presence of halide ions in solution, such as $Cl^-(aq)$, increase their corrosion inhibitor performance [1,2]. Moreover, it is suggested (see, for example Ref. [36]) that this enhancement arises through surface bound halide (e.g. Cl_{ads}) acting as a bridge to facilitate the binding of positively charged

corrosion inhibitors to the substrate. Given that we have concluded here that adsorbed OMID is singly protonated, such a bonding mode is feasible, i.e. $OMIDH^+$ - Cl_{ads} – Fe. It should be emphasised, however, that this possibility remains conjecture, and further effort is required to gain proof.

Conclusions

In summary, a combination of electrochemical measurements and interface analysis have been applied to elucidate the functionality OMID as a corrosion inhibitor for carbon steel in aqueous 1 M HCl at room temperature (25°C). It is demonstrated that the addition of 0.01 mM OMID delivers excellent corrosion inhibition efficiency i.e. $\eta\% > 95\%$. Moreover, this concentration is more than one order of magnitude below the CMC of OMID in this medium. XPS spectra indicate that OMID adsorbs, as described previously [11], in two different singly protonated forms, and that interface chemistry varies as a function of environment. Most notably, the coverage of a surface salt film (iron chloride) diminishes as OMID concentration increases, and OMID is bound to film-free carbon steel on a highly inhibited substrate. Finally, evidence derived from Cl 2p XPS line shape analysis of Cl_{ads} suggests a heterogeneous substrate termination at lower OMID concentrations, consisting of filmed and film-free domains.

Acknowledgements

Funding and technical support from AkzoNobel and Nouryon through a collaboration with The University of Manchester is acknowledged. KK is appreciative of funding from the EPSRC (EP/L01680X/1) through the Materials for Demanding Environments (M4DE) Centre for Doctoral Training (CDT). Furthermore, we are grateful for additional funding and technical support from BP through the BP International Centre for Advanced Materials (BP-ICAM) and EPSRC through the prosperity partnership (EP/G036850/1).

Data Availability

The raw data required to reproduce these findings are available to download from http://dx.doi.org/10.17632/dv5jvpjkg7.1 [40].

References

[1] M. Finšgar, J. Jackson, Application of corrosion inhibitors for steels in acidic media for the oil and gas industry: A review, Corros. Sci. 86 (2014) 17–41. https://doi.org/10.1016/j.corsci.2014.04.044.

[2] Y. Zhu, M.L. Free, R. Woollam, W. Durnie, A review of surfactants as corrosion inhibitors and associated modeling, Prog. Mater. Sci. 90 (2017) 159–223. https://doi.org/10.1016/j.pmatsci.2017.07.006.

[3] D. Klenerman, J. Hodge, M. Joseph, Second Harmonic Generation at Surfaces Applied to Corrosion Inhibition, Corros. Sci. 36 (1994) 301–313.

[4] A. Edwards, C. Osborne, S. Webster, D. Klenerman, M. Joseph, P. Ostovar, M. Doyle, Mechanistic studies of the corrosion inhibitor oleic imidazoline, Corros. Sci. 36 (1994) 315–325. https://doi.org/10.1016/0010-938X(94)90160-0.

[5] S. Ramachandran, B.-L. Tsai, M. Blanco, H. Chen, Y. Tang, W.A. Goddard, Self-Assembled Monolayer Mechanism for Corrosion Inhibition of Iron by Imidazolines, Langmuir. 12 (1996) 6419–6428. https://doi.org/10.1021/la960646y.

[6] S.T. Keera, N.A. Farid, K.Z. Mohamed, Imidazoline Derivatives as Corrosion Inhibitors of Carbon Steel in Crude Oils and Associated Water, Energy Sources Part Recovery Util. Environ. Eff. 34 (2012) 1371–1383. https://doi.org/10.1080/15567036.2010.481657.

[7] O. Olivares-Xometl, N.V. Likhanova, M.A. Domínguez-Aguilar, J.M. Hallen, L.S. Zamudio, E. Arce, Surface analysis of inhibitor films formed by imidazolines and amides on mild steel in an acidic environment, Appl. Surf. Sci. 252 (2006) 2139–2152. https://doi.org/10.1016/j.apsusc.2005.03.178.

[8] O. Olivares-Xometl, N.V. Likhanova, R. Martínez-Palou, M.A. Domínguez-Aguilar, Electrochemistry and XPS study of an imidazoline as corrosion inhibitor of mild steel in an acidic environment, Mater. Corros. 60 (2009) 14–21. https://doi.org/10.1002/maco.200805044.

[9] J. Zhao, G. Chen, The synergistic inhibition effect of oleic-based imidazoline and sodium benzoate on mild steel corrosion in a CO_2-saturated brine solution, Electrochim. Acta. 69 (2012) 247–255. https://doi.org/10.1016/j.electacta.2012.02.101.

[10] M. Yadav, D. Behera, U. Sharma, Nontoxic corrosion inhibitors for N80 steel in hydrochloric acid, Arab. J. Chem. 9 (2016) S1487–S1495. https://doi.org/10.1016/j.arabjc.2012.03.011.

[11] K. Kousar, T. Ljungdahl, A. Wetzel, M. Dowhyj, H. Oskarsson, A.S. Walton, M.S. Walczak, R. Lindsay, An Exemplar Imidazoline Surfactant for Corrosion Inhibitor Studies: Synthesis, Characterization, and Physicochemical Properties, J. Surfactants Deterg. 23 (2020) 225–234. https://doi.org/10.1002/jsde.12363.

[12] M.S. Walczak, P. Morales-Gil, T. Belashehr, K. Kousar, P. Arellanes Lozada, R. Lindsay, Determining the Chemical Composition of Corrosion Inhibitor/Metal Interfaces with XPS: Minimizing Post Immersion Oxidation, J. Vis. Exp. (2017) 55163. https://doi.org/10.3791/55163.

[13] R.A. Cottis, Electrochemical Methods, in: R. A. Cottis, M.J. Graham, R. Lindsay, S.B. Lyon, J.A. Richardson, J.D. Scantlebury, F.H. Stott (Eds.), Shreir's Corrosion, vol. 2, Corrosion in Liquids, Corrosion Evaluation, Elsevier, Amsterdam, 2010, pp. 1341-1373.

[14] W. Oelßner, F. Berthold, U. Guth, The iR drop - well-known but often underestimated in electrochemical polarization measurements and corrosion testing, Mater. Corros. 57 (2006) 455–466. https://doi.org/10.1002/maco.200603982.

[15] Thermoscientific XPS Simplified. https://xpssimplified.com/elements/iron.php (accessed September 13, 2020).

[16] Casa Software Ltd, Teignmouth, Devon, UK. http://www.casaxps.com/ (accessed September 14, 2020).

[17] P. Morales-Gil, M.S. Walczak, R.A. Cottis, J.M. Romero, R. Lindsay, Corrosion inhibitor binding in an acidic medium: Interaction of 2-mercaptobenizmidazole with carbon-steel in hydrochloric acid, Corros. Sci. 85 (2014) 109–114. https://doi.org/10.1016/j.corsci.2014.04.003.

[18] P. Morales-Gil, M.S. Walczak, C.R. Camargo, R.A. Cottis, J.M. Romero, R. Lindsay, Corrosion inhibition of carbon-steel with 2-mercaptobenzimidazole in hydrochloric acid, Corros. Sci. 101 (2015) 47–55. https://doi.org/10.1016/j.corsci.2015.08.032.

[19] R.P. Gupta, S.K. Sen, Calculation of multiplet structure of core p -vacancy levels. II, Phys. Rev. B. 12 (1975) 15–19. https://doi.org/10.1103/PhysRevB.12.15.

[20] N. Fairley, CasaXPS Manual 2.3.15 Spectroscopy 1.3, Casa Software Ltd, 2009.

[21] D.A. Shirley, High-Resolution X-Ray Photoemission Spectrum of the Valence Bands of Gold, Phys. Rev. B. 5 (1972) 4709–4714. https://doi.org/10.1103/PhysRevB.5.4709.

[22] S. Doniach, M. Sunjic, Many-electron singularity in X-ray photoemission and X-ray line spectra from metals, J. Phys. C Solid State Phys. 3 (1970) 285–291. https://doi.org/10.1088/0022-3719/3/2/010.

[23] G. Wertheim, P. Citrin, Fermi Surface Excitations in X-ray Photoemission Line Shapes from Metals, in: M. Cardona, L. Ley (Eds.), Top. Appl. Phys. Photoemiss. Solids Gen. Princ., Springer-Verlag, Berlin, Heidelberg, New York, 1978: pp. 197–236.

[24] M.J. Acres, H. Hussain, M.S. Walczak, M. Nikiel, C. Sewell, C. Rafols i Belles, E.A. Ahmad, A.S. Walton, C.A. Muryn, N.M. Harrison, R. Lindsay, Core level photoemission line shape selection: Atomic adsorbates on iron, Surf. Interface Anal. 52 (2020) 507–512. https://doi.org/10.1002/sia.6770.

[25] R. Dovesi, V. Saunders, C. Roetti, R. Orlando, C. Zicovich-Wilson, F. Pascale, B. Civalleri, K. Doll, N. Harrison, I. Bush, P. D'Arco, M. Llunell, M. Causà, Y. Noël, L. Maschio, A. Erba, M. Rerat, S. Casassa, CRYSTAL17 User's Manual, (2017).

[26] R. Dovesi, A. Erba, R. Orlando, C.M. Zicovich-Wilson, B. Civalleri, L. Maschio, M. Rérat, S. Casassa, J. Baima, S. Salustro, B. Kirtman, Quantum-mechanical condensed matter simulations with CRYSTAL, Wiley Interdiscip. Rev. Comput. Mol. Sci. 8 (2018) e1360. https://doi.org/10.1002/wcms.1360.

[27] R. Lindsay, S.B. Lyon, Introduction to Control of Corrosion by Environmental Control, in: R. A. Cottis, M.J. Graham, R. Lindsay, S.B. Lyon, J.A. Richardson, J.D. Scantlebury, F.H. Stott (Eds.), Shreir's Corrosion, vol. 4, Management and Control of Corrosion, Elsevier, Amsterdam, 2010, pp. 2891-2899.

[28] M.S. Walczak, P. Morales-Gil, R. Lindsay, Determining Gibbs energies of adsorption from corrosion inhibition efficiencies: Is it a reliable approach?, Corros. Sci. 155 (2019) 182–185. https://doi.org/10.1016/j.corsci.2019.04.040.

[29] Y. Zhu, M.L. Free, G. Yi, Experimental Investigation and Modeling of the Performance of Pure and Mixed Surfactant Inhibitors: Aggregation, Adsorption, and Corrosion Inhibition on Steel Pipe in Aqueous Phase, J. Electrochem. Soc. 162 (2015) C582–C591. https://doi.org/10.1149/2.09415010jes.

[30] Y. Zhu, M.L. Free, G. Yi, Electrochemical measurement, modeling, and prediction of corrosion inhibition efficiency of ternary mixtures of homologous surfactants in salt solution, Corros. Sci. 98 (2015) 417–429. https://doi.org/10.1016/j.corsci.2015.05.050.

[31] Y. Zhu, M.L. Free, G. Yi, The effects of surfactant concentration, adsorption, aggregation, and solution conditions on steel corrosion inhibition and associated modeling in aqueous media, Corros. Sci. 102 (2016) 233–250. https://doi.org/10.1016/j.corsci.2015.10.012.

[32] E. Tyrode, M.W. Rutland, C.D. Bain, Adsorption of CTAB on Hydrophilic Silica Studied by Linear and Nonlinear Optical Spectroscopy, J. Am. Chem. Soc. 130 (2008) 17434–17445. https://doi.org/10.1021/ja805169z.

[33] A.A. Al-Refaie, J. Walton, R.A. Cottis, R. Lindsay, Photoelectron spectroscopy study of the inhibition of mild steel corrosion by molybdate and nitrite anions, Corros. Sci. 52 (2010) 422–428. https://doi.org/10.1016/j.corsci.2009.09.030.

[34] G.C. Smith, Evaluation of a simple correction for the hydrocarbon contamination layer in quantitative surface analysis by XPS, J. Electron Spectrosc. Relat. Phenom. 148 (2005) 21–28. https://doi.org/10.1016/j.elspec.2005.02.004.

[35] A.P. Grosvenor, B.A. Kobe, M.C. Biesinger, N.S. McIntyre, Investigation of multiplet splitting of Fe 2p XPS spectra and bonding in iron compounds, Surf. Interface Anal. 36 (2004) 1564–1574. https://doi.org/10.1002/sia.1984.

[36] P. Arellanes-Lozada, O. Olivares-Xometl, N.V. Likhanova, I.V. Lijanova, J.R. Vargas-García, R.E. Hernández-Ramírez, Adsorption and performance of ammonium-based

ionic liquids as corrosion inhibitors of steel, J. Mol. Liq. 265 (2018) 151–163. https://doi.org/10.1016/j.molliq.2018.04.153.

[37] A.M. Al-Fakih, H.H. Abdallah, M. Aziz, Experimental and theoretical studies of the inhibition performance of two furan derivatives on mild steel corrosion in acidic medium, Mater. Corros. 70 (2019) 135–148. https://doi.org/10.1002/maco.201810221.

[38] J. Haque, V. Srivastava, M.A. Quraishi, D. Singh Chauhan, H. Lgaz, I.-M. Chung, Polar group substituted imidazolium zwitterions as eco-friendly corrosion inhibitors for mild steel in acid solution, Corros. Sci. 172 (2020) 108665. https://doi.org/10.1016/j.corsci.2020.108665.

[39] Y. Kharbach, F.Z. Qachchachi, A. Haoudi, M. Tourabi, A. Zarrouk, C. Jama, L.O. Olasunkanmi, E.E. Ebenso, F. Bentiss, Anticorrosion performance of three newly synthesized isatin derivatives on carbon steel in hydrochloric acid pickling environment: Electrochemical, surface and theoretical studies, J. Mol. Liq. 246 (2017) 302–316. https://doi.org/10.1016/j.molliq.2017.09.057.

[40] K. Kousar, M.S. Walczak, T. Ljungdahl, A. Wetzel, H. Oskarsson, P. Restuccia, E.A. Ahmad, N.M. Harrison, R. Lindsay, Data for Corrosion inhibition of carbon steel in hydrochloric acid: Elucidating the performance of an imidazoline-based surfactant", Mendeley Data, V1, 2020, doi: 10.17632/dv5jvpjkg7.1.

Figure Captions

Fig. 1 A ball and stick model of OMID ((Z)-2-(2-(heptadec-8-en-1-yl)-4,5-dihydro-1H-imidazol-1-yl)ethan-1-amine). The fragment labelled *Head Group* comprises a heterocyclic ring ($C_3N_2H_4$) and a pendant side group ($C_2H_4NH_2$). The *Tail Group* is an unbranched aliphatic chain ($C_{17}H_{33}$).

Fig. 2 PDP curves acquired from carbon steel after 4 h immersion in *1 M HCl + x mM OMID, where x =* 0 mM, 0.0001 mM, 0.001 mM, 0.005 mM, and 0.1 mM.

Fig. 3 Mean corrosion rates (red markers) and η%'s (blue markers) plotted as a function of OMID concentration; the dashed red and blue lines have been inserted to guide the eye. Each mean value has been derived from at least two independent LPR measurements, acquired from carbon steel after immersion for 4 h in *1 M HCl + x mM OMID,* and the associated error bar denotes the standard deviation. η% = 95% is indicated by a horizontal dashed grey line. The vertical dashed grey line marks the CMC of OMID in 1 M HCl at room temperature [11].

Fig. 4 SEM images (secondary electron mode) of carbon steel samples, acquired following the removal of any adhered corrosion scale: (a) polished; (b) subsequent to immersion for 4 h in *1 M HCl + 0 mM OMID*; (c) subsequent to immersion for 4 h in *1 M HCl + 0.1 mM OMID*.

Fig. 5 Overview XPS spectra ($h\nu$ = 1486.6 eV, $\theta_E = 0°$) acquired from carbon steel subsequent to immersion for 4 h in *1 M HCl + x mM OMID*. The bottommost spectrum was acquired from a polished substrate. Each spectrum has been normalised using the total peak area of the Fe $2p_{3/2}$ signal.

Fig. 6 N 1s core level XPS data (hν = 1486.6 eV, θ_E = 0°) acquired from carbon steel subsequent to immersion for 4 h in *1 M HCl + x mM OMID*. The bottommost spectrum was acquired from a polished substrate. Each spectrum has been normalised using the total peak area of the Fe $2p_{3/2}$ components extracted from the corresponding Fe 2p spectrum. Blue markers show best fits to the experimental spectra (solid black lines), using GL (red lines) and Shirley-type (broken grey lines) functions. Peak assignments, consistent with OMID adsorbed in the two singly protonated forms depicted in this figure, are also indicated. R = $C_{17}H_{33}$.

Fig. 7 (a) Fe 2p, (b) O 1s, and (c) Cl 2p core level XPS spectra (hν = 1486.6 eV, θ_E = 0°) acquired from carbon steel subsequent to immersion for 4 h in *1 M HCl + x mM OMID*. The bottommost spectrum in each panel was acquired from a polished substrate. Each spectrum has been normalised using the total peak area of the Fe $2p_{3/2}$ components extracted from the corresponding Fe 2p spectrum. Blue markers show best fits to the experimental spectra (solid black lines), using GL (red lines), LF (red lines), and Shirley-type (broken grey lines) functions. Peak assignments are also indicated. For the Cl 2p spin-orbit split doublets (Cl $2p_{1/2}$ and Cl$2p_{3/2}$), the BE difference and intensity ratio were fixed at expected values [16,17].

Fig. 8 To the left, structure of ordered (2x2) overlayer of Cl atoms on Fe(110) (plan and side views) optimised in DFT calculations to produce DFT-PDOS for Cl, Fe1, Fe2, and Fe3 (see labels in side view). The indicated Cl adsorption site was found to be the most favourable of those tested during DFT modelling of a 5 layer Fe(110)(2x2)-Cl slab. To the right, the corresponding DFT-PDOS (-2 eV ≤ E_F ≤ 2 eV) are plotted.

Fig. 9 Series of cartoons depicting the termination of carbon steel as a function of *1 M HCl + x mM OMID,* as derived from XPS data*;* the leftmost cartoon shows a polished substrate. It should be pointed out that the lateral locations of some species cannot be identified. For example, as shown here, OMID may adsorb only on film-free areas of the surface for *1 M HCl + ≤ 0.005 mM OMID*, or also atop patches of iron chloride.

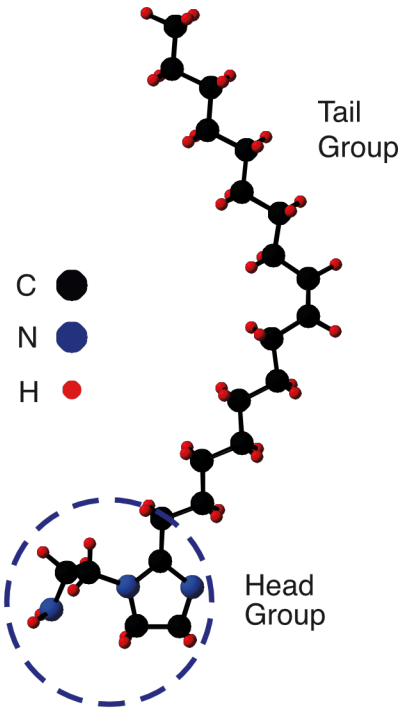


Figure 1

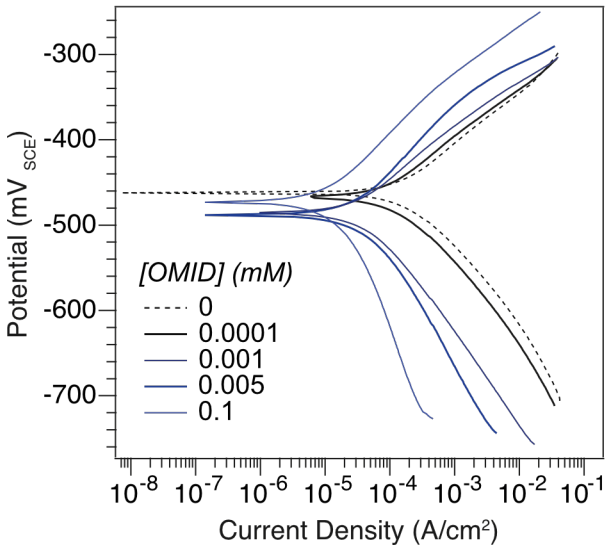

-300
-400
-500
-600
-700
Potential (mV SCE)
[OMID] (mM)
0
0.0001
0.001
0.005
0.1
10-8 10-7 10-6 10-5 10-4 10-3 10-2 10-1
Current Density (A/cm2)

Figure 2

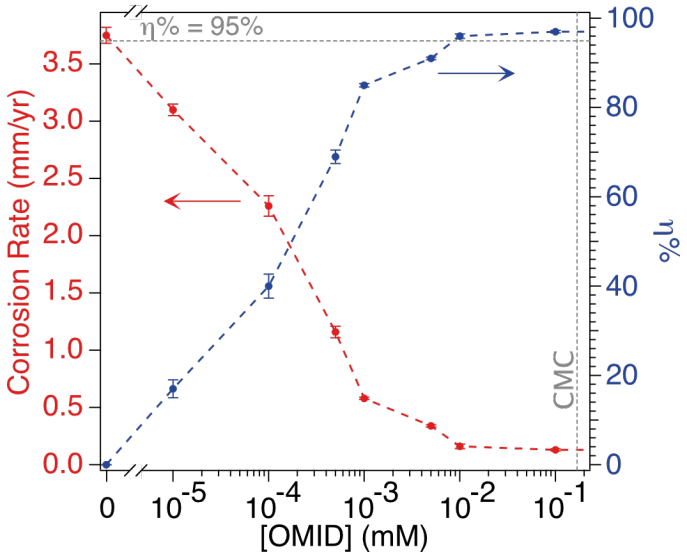

η% = 95%
Corrosion Rate (mm/yr)
%η
CMC
[OMID] (mM)
0
10-5
10-4
10-3
10-2
10-1
0.0
0.5
1.0
1.5
2.0
2.5
3.0
3.5
0
20
40
60
80
100

Figure 3

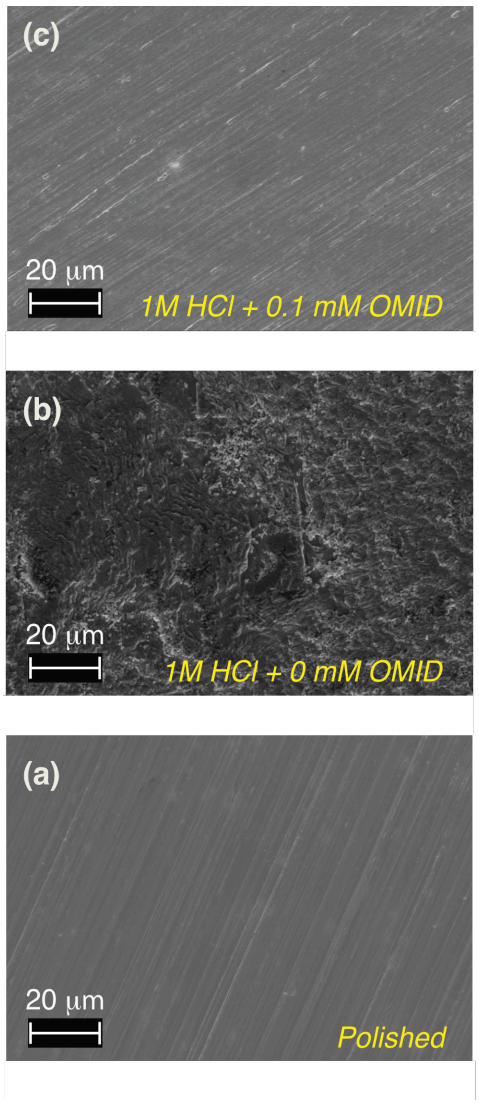


Figure 4

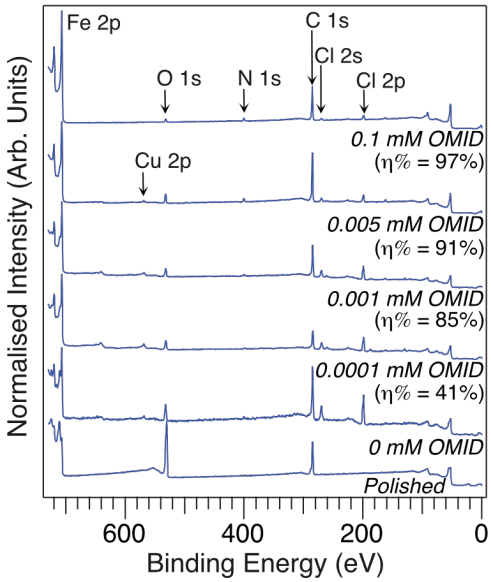

Fe 2p
C 1s
Cl 2s
O 1s
N 1s
Cl 2p
0.1 mM OMID
(η% = 97%)
Cu 2p
0.005 mM OMID
(η% = 91%)
0.001 mM OMID
(η% = 85%)
0.0001 mM OMID
(η% = 41%)
0 mM OMID
Polished
Normalised Intensity (Arb. Units)
600
400
200
0
Binding Energy (eV)

Figure 5

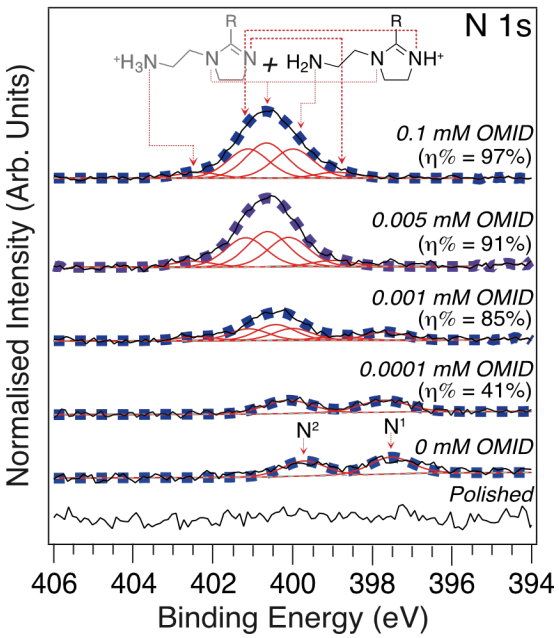

N 1s
0.1 mM OMID
(η% = 97%)
0.005 mM OMID
(η% = 91%)
0.001 mM OMID
(η% = 85%)
0.0001 mM OMID
(η% = 41%)
N²
N¹
0 mM OMID
Polished
Normalised Intensity (Arb. Units)
406
404
402
400
398
396
394
Binding Energy (eV)

Figure 6

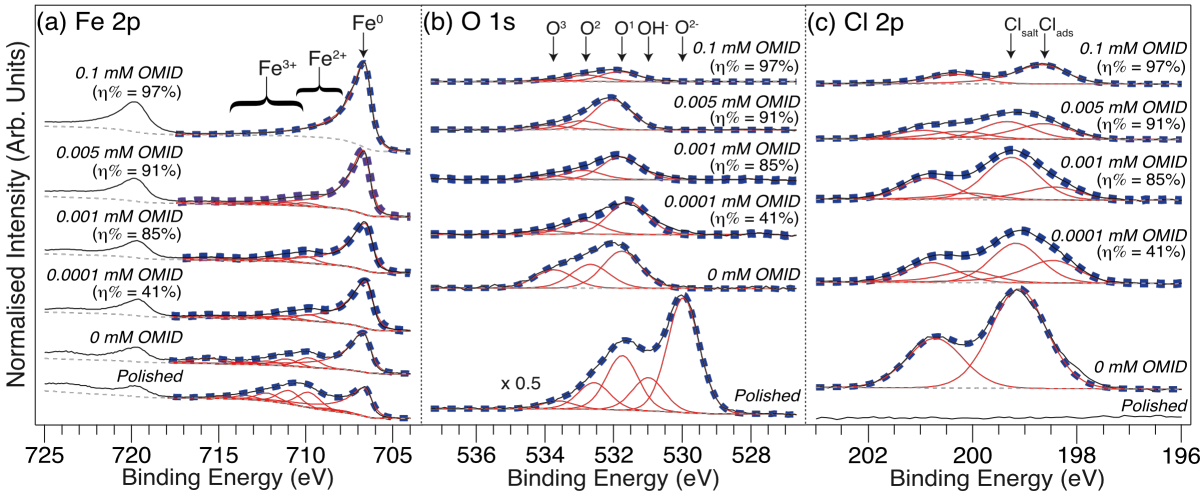

(a) Fe 2p
Fe0
Fe3+
Fe2+
0.1 mM OMID
(η% = 97%)
0.005 mM OMID
(η% = 91%)
0.001 mM OMID
(η% = 85%)
0.0001 mM OMID
(η% = 41%)
0 mM OMID
Polished
Normalised Intensity (Arb. Units)
725
720
715
710
705
Binding Energy (eV)
(b) O 1s
O3
O2
O1
OH-
O2-
x 0.5
536
534
532
530
528
Binding Energy (eV)
(c) Cl 2p
Cl salt
Cl ads
202
200
198
196
Binding Energy (eV)

Figure 7

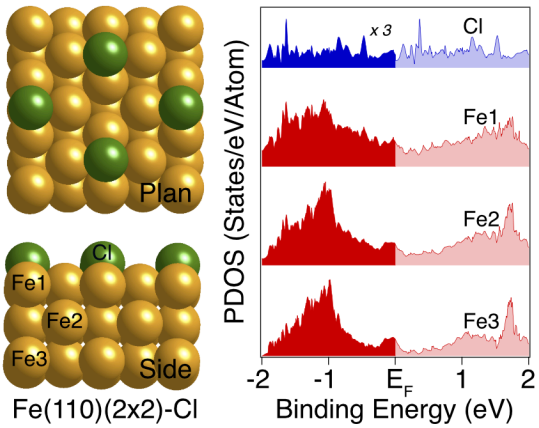

Plan
Cl
Fe1
Fe2
Fe3
Side
Fe(110)(2x2)-Cl
x 3
Cl
Fe1
Fe2
Fe3
PDOS (States/eV/Atom)
-2
-1
E_F
1
2
Binding Energy (eV)

Figure 8

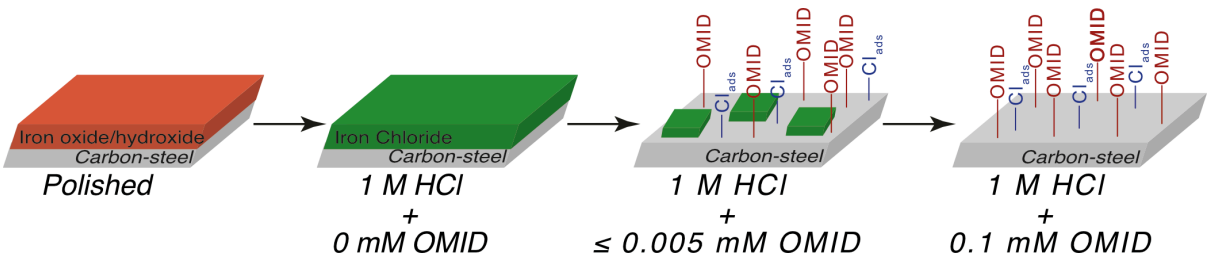

Iron oxide/hydroxide
Carbon-steel
Polished
Iron Chloride
Carbon-steel
1 M HCl
+
0 mM OMID
Carbon-steel
1 M HCl
+
≤ 0.005 mM OMID
Carbon-steel
1 M HCl
+
0.1 mM OMID

Figure 9